Precision Agriculture (2026) 27:62
https://doi.org/10.1007/s11119-026-10368-z

Machine learning-enhanced UAV multispectral remote sensing for monitoring rice leaf area index across critical growth stages

Chao Su[1] · Zaiying Ling[1] · Liwang Han[1] · Yanmin Shuai[2] · Jianguang Wen[3] · Xingwen Lin[2] · Haifeng Tang[4] · Alexandre Maniçoba da Rosa Ferraz Jardim[5] · Hoi Leong Lee[6] · Xuguang Tang[1]

Received: 27 August 2025 / Accepted: 27 April 2026

Abstract
Purpose Traditional methods struggle to accurately and efficiently monitor rice leaf area index (LAI) throughout the entire growth period, hindering precision agriculture management.
Methods To address this problem, this study integrated unmanned aerial vehicle (UAV) multi-spectral remote sensing with machine learning to develop a novel model for dynamic rice LAI monitoring in Zhejiang province, China, leveraging data from critical stages including tillering, jointing, and heading. Then, the normalized difference vegetation index (NDVI), the normalized green-red difference index (NGRDI), the normalized difference red edge index (NDRE), the red-edge ratio vegetation index (RERVI) and the enhanced vegetation index (EVI) were calculated. On this basis, linear and nonlinear models using single vegetation index were constructed separately. Additionally, two empirical models including the partial least squares regression (PLSR) and the ridge regression (RR), and four machine learning models including the random forest (RF), the support vector machine (SVM), the k-nearest neighbor (kNN) and the improved feed forward neural network (FNN) were developed utilizing five vegetation indices.
Results The results indicated that among the traditional empirical models, the nonlinear model LAI-EVI$_{\text{non-linear}}$ performed the best, with R^2 of 0.756 and RMSE of 0.680, which also suggested that incorporating more vegetation indices as input data did not necessarily effectively improve the inversion accuracy by the PLSRand RR models. However, the performances of four machine learning models exhibited significant improvements. The LAIFNN model achievedthe highest accuracy, with R^2 and RMSE by about 0.821 and 0.583, respectively. The contribution of each input feature was also quantified byusing the SHapley Additive exPlanations (SHAP) method. Based on the optimal model, this study mapped the multi-temporal spatial patterns ofrice LAI.
Conclusion These findings implied that the UAV-based remote sensing combined with high-performance machine learning offers apractical approach for LAI monitoring of the rice agro-ecosystem.

Extended author information available on the last page of the article

Keywords LAI · Machine learning · Precision agriculture · Rice · UAV

Introduction

Rice is one of the most important cereal crops in the world, with about half of the global population relying on rice as staple food, which is critical for ensuring food security (Bandumula, 2018; Chen et al., 2022). Since 2010, the total rice cultivation area worldwide has kept relatively stable, amounting to roughly 160 million ha, with the majority distributed in the monsoon-prone regions of East Asia, Southeast Asia, and South Asia (Lin et al., 2022a, 2022b; Shaheen et al., 2022; Yuan et al., 2022). As a reliable indicator for characterizing the growth status of crops, leaf area index (LAI) refers to the ratio of the total area of plant leaves to the land area per square meter (Colombo et al., 2003; Raj et al., 2021). Accurate monitoring of LAI dynamics is indispensable for deciphering rice growth trajectories, forecasting yield, assessing environmental fitness, and formulating precise, site-specific management strategies that both boost production and propel agriculture toward smart, precision-driven systems.

The traditional method of LAI monitoring typically involves ground-based measurements (Woodgate et al., 2015). While this method provides accurate and reliable LAI data, it is time-consuming, labor-intensive, and limited to small areas. Therefore, it is not suitable for large-scale or repeated monitoring. In recent years, with the development of satellite remote sensing technology, it has become a feasible way to monitor and assess crop LAI frequently over a large scale, with high efficiency and non-destructively, which can also lower the costs relatively to ground-based measurements (Bajocco et al., 2022; Wang & Fang, 2020). However, the satellite-based methods for LAI retrieval are subject to certain limitations, for example, the accuracy may be affected by factors such as cloud cover, atmospheric conditions and satellite resolution, as well as the inversion methods (Chen et al., 2025; Dhakar et al., 2021; Sun et al., 2023). Specifically, despite that plenty of studies have used the Landsat, Sentinel, and MODIS as data sources for estimating crop LAI (Luo et al., 2020a, 2020b; Sun et al., 2021; Xiao et al., 2016), satellites with long revisit times often struggle to collect enough cloud-free observations during crop growing season, leading to large uncertainties in model parameterization and increased errors in crop LAI estimates. Alternatively, the unmanned aerial vehicle (UAV) equipped with multispectral or hyperspectral sensors can be used to collect high-resolution imagery of crop fields (Gao et al., 2016; Li et al., 2019; Prabhakar et al., 2024). Recent work by Vishwakarma et al. (2025) demonstrated machine learning framework for estimating rice LAI across multiple growth stages using UAV multispectral data. This technology offers low cost, high spatial and temporal resolution, and enhanced flexibility. Meanwhile, these images can be processed to calculate various vegetation indices and estimate LAI with greater accuracy and higher resolution than satellite imagery. The application of this technology opens up new possibilities for precise agricultural management, providing more accurate data for agricultural production monitoring and decision-making.

The main LAI inversion models are encompassed of empirical models, physical models, and machine learning models. The physical models used to retrieve LAI are based on the principles of radiative transfer theory (Jiang et al., 2023; Kimm et al., 2020). These models simulate the interaction between solar radiation and the vegetation canopy, taking into account factors such as leaf optical properties, canopy structure, and soil reflectance. But such model can be highly complex and computationally intensive, and sensitive to input parameter accuracy, while the empirical model is simpler and easier. The method usually uses the spectral reflectance or vegetation index as the independent variable, and crop LAI as the dependent variable, and builds up the estimation model through statistical analyses (Kang et al., 2016). In terms of independent variable selection, several vegetation indices evolved from spectral information, such as the normalized difference vegetation index (NDVI), the visible-band difference vegetation index (VDVI), the normalized green–red difference index (NGRDI), the normalized difference red edge index (NDRE), the red-edge ratio vegetation index (RERVI), the modified green–red vegetation index (MGRVI) and the enhanced vegetation index (EVI), have performed well in inversion studies (Barrero & Perdomo, 2018; Hammond et al., 2023; Xu et al., 2020). Nevertheless, such method has limited ability to capture complex relationships between remote sensing data and LAI. However, machine learning algorithms can be used to monitor crop physiological and biochemical parameters, as they can enhance the estimation accuracy by learning the complex non-linear relationships within remote sensing data (Ahmad et al., 2023; Papapicco et al., 2022; Zhang et al., 2021). Currently, researches using UAV remote sensing technology to predict LAI is increasingly gaining attention. Plenty of studies have shown that high-resolution image data acquired via UAVs can effectively predict crop LAI (Cheng et al., 2024; Fei et al., 2023).

However, due to the distinct characteristics of the paddy field environment, particularly during certain growth stages in contrast to upland crops like wheat and corn, in field collection of LAI data presents significant challenges. Consequently, most existing studies have focused on static modeling for single growth stage, such as the jointing or heading stage (Han et al., 2025; Nazir et al., 2021). This approach not only limits the temporal representativeness of the models but also hinders their ability to support precision agricultural decisions requiring dynamic monitoring across the entire growth cycle. Although machine learning methods have been widely applied in vegetation parameter retrieval, many deep learning models used for rice LAI estimation are structurally complex and prone to overfitting when trained on small sample sizes (Sun et al., 2024). Nevertheless, the full potential of advanced machine learning, especially deep learning algorithms, remains largely untapped for UAV based LAI retrieval, indicating substantial room for methodological breakthroughs.

Against this backdrop, the study collected the UAV-based multispectral imagery and corresponding ground based LAI measurements across three critical growth stages of rice including the tillering, jointing, and heading. This allowed us to build a continuous dataset that captures the core phases of the entire growth cycle, moving beyond the constraints of traditional single stage modeling and enabling the tracking of LAI dynamics over time. At the methodological level, we systematically evaluated the potential of multiple empirical models and machine learning algorithms for rice LAI retrieval, and structurally optimized the traditional FNN. By incorporating residual connections and batch normalization layers, we constructed a lightweight network architecture that combines structural simplicity and strong generalization capability. This approach effectively addresses the issues of model overfitting and insufficient representational capacity in small-sample rice remote sensing scenarios. The monitoring setup and optimal model from this study can be quickly used for ongoing rice growth monitoring. They can measure rice growth details, give farmland managers fast and effective LAI information, and provide scientific support for farmland fertilization and irrigation actions. Building upon this innovative framework, this study specifically aims to accomplish the following objectives: (1) construct and evaluate the linear and nonlinear rice LAI estimation models based on single vegetation index including NDVI, NDRGI, NDRE, RERVI and EVI; (2) examine the performances of four machine learning models including the random forest (RF), support vector machine (SVM), k-nearest neighbor (kNN), improved feedforward neural network (FNN) and two empirical models including the partial least squares regression (PLSR), the ridge regression (RR) by incorporating five vegetation indices; (3) to interpret the optimal inversion model by using the the Shapley additive explanations (SHAP) algorithm, and then map the spatial patterns of rice LAI throughout the growth period.

Materials and methods

Description of the study area

The comprehensive observation site of the farmland ecosystem of Hangzhou Normal University is located in Shaoxing City, Zhejiang Province, China (120°30’E, 29°58’N). The area has a subtropical monsoon climate with four distinct seasons, abundant rainfall, and a mild and humid climate. The annual average temperature is about 16 ℃ to 18 ℃, and the annual precipitation can reach more than 1,400 mm. Typically, this area experiences higher precipitation during spring and summer, due to monsoon influences and other meteorological factors. The land has flat terrain and is primarily used for field crops. The water and heat conditions are suitable for double-cropping rice cultivation (Luo et al., 2020a, 2020b). As shown in Fig. 1, the total area of the study area is approximately 85 ha, of which the rice planting area is 66 ha, accounting for about 78%. Two sowing methods are employed in the study area including the mechanical transplanting, in which nursery-raised seedlings are transplanted into the paddy by the rice transplanter, and UAV direct seeding, wherein rice seeds are aerially broadcast. The rice cultivar ‘Zhongzu 53’ was grown throughout the study area, with mechanical transplanting performed on 20 April 2024 using a planting spacing of 25 cm between rows and 18 cm within rows. Fertilizer was applied at three growth stages: after sowing, during the mid-tillering stage, and at the pre-jointing stage. Harvesting took place on 15 July 2024.

Rice LAI measurement

After rice transplanting, this study selected the clear and cloudless days to conduct ground experiments including the LAI measurement and the UAV flight at three critical growth stages: the tillering stage (2024—05—09), the jointing stage (2024—06—03), and the heading stage (2024—07—04). The observation time of rice LAI is chosen after sunset to avoid the influence of direct sunlight. As a highly specialized piece of equipment designed to measure the structural characteristics of plant canopies, the LAI-2200C Plant Canopy Analyzer, manufactured by LI-COR in the United States, is used to acquire the in situ LAI data. This device uses its "fisheye" optical sensor to measure the changes in light intensity inside and outside the rice canopy from five zenith angles of 7°, 23°, 38°, 53°, and 68°, and calculates LAI of the rice canopy through a radiation propagation model (Fang et al., 2014). During measurement, we randomly select the measurement points in the paddy field, ensur-

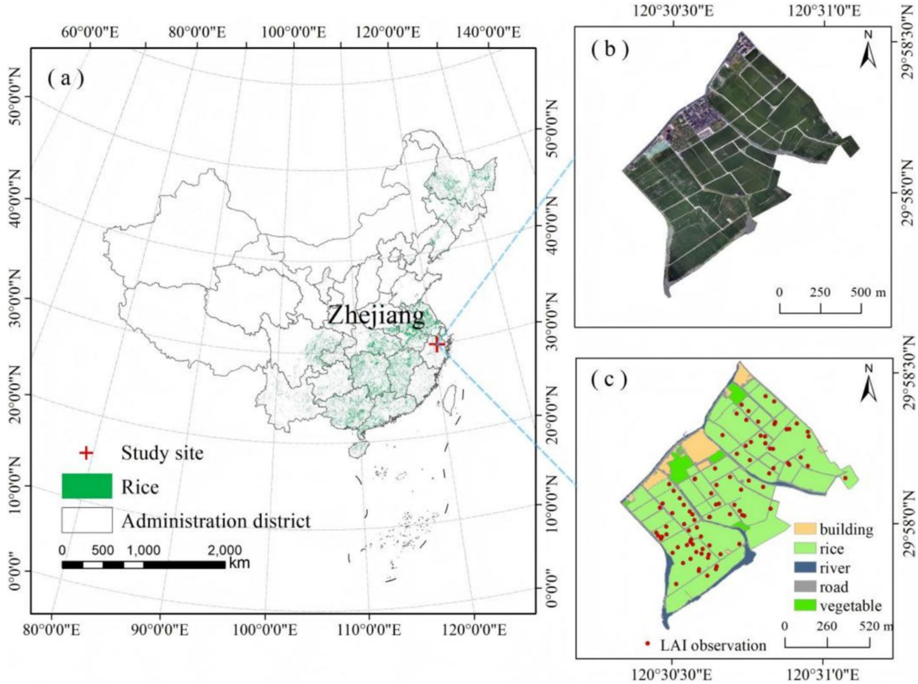

Fig. 1 (**a**) The geographic location of the study area in Zhejiang Province, China. (**b**) True-color orthomosaic of the study area acquired by UAV. (**c**) Land cover classification map (green: rice planting area) with overlaid locations of LAI observation collected at the tillering, jointing, and heading stages. The geographic coordinate system in use is GCS_WGS_1984, while the projected coordinate system is set as WGS_1984_UTM_Zone_50N (Color figure online)

ing a uniform distribution that can reflect the overall growth condition of the rice. When measuring, one A value and four B values should be determined. The A value is measured directly above the rice canopy. The B value is measured in the diagonal direction between the two rows of rice, as follows: the first B value is located directly below the single-row rice; the second B value is located at 1/4 of the ridge; the third B value is located at 1/2 of the ridge; and the last B value is 3/4 of the way down the ridge.

To systematically capture the spatial heterogeneity of rice canopy conditions within the study area and their temporal dynamics across different growth stages, this study adopted a completely independent sampling strategy throughout the growing season. Specifically, during the three ground-based sampling campaigns corresponding to the tillering, jointing, and heading stages, these sampling points were distributed across distinct spatial locations (30, 35, and 30 points, respectively). This resulted in a total of 95 independent LAI measurements from unique geographical locations over the entire growing season, as visualized in Fig. 1c. This design enables the characterization of spatial variability within each growth stage while facilitating the assessment of regional-scale growth dynamics through cross-stage comparisons.

UAV multi-spectral data acquisition and processing

The flight experiment was conducted concurrently with the ground LAI experiment. The study utilized the Matrice M300 RTK UAV, manufactured by China's DJI, as the airborne platform, and the RedEdge-MX multispectral camera produced by the US company MICA-SENSE was equipped. This multispectral camera comprises of five bands including the blue, green, red, red edge, and near-infrared, which enable accurate and flexible estimation of the physiological and biochemical parameters of crops (Liu et al., 2022a, 2022b, 2022c). Detailed information about the bands were presented in Table 1. The flight was conducted at an altitude of 200 m and a speed of 7 m/s, with 75% front overlap and 80% side overlap. This configuration resulted in a ground sampling distance (GSD) of 0.08 m, providing high resolution coverage of the study area in an efficient manner.

The stitching and processing of UAV multispectral imagery were completed using the Agisoft Metashape Professional software. The workflow began with importing the raw images from the five spectral bands, after which the software automatically aligns the bands based on embedded metadata. Radiometric calibration was then performed by converting raw digital numbers to surface reflectance using images of a laboratory calibrated spectral diffuse reflectance panel captured under natural lighting conditions before and after the flight. For geometric correction, the Matrice 300 RTK platform, equipped with a built in high precision GNSS module, provides centimeter level initial positioning. This was further refined using five ground control points strategically placed around the perimeter and at the center of the study area, surveyed with differential GNSS, to optimize the exterior orientation parameters from the onboard RTK GNSS. Bundle adjustment was then applied to enhance camera parameters and image positions. Finally, band specific reflectance values were extracted through raster calculation, and vegetation indices were computed for subsequent analysis. The bundle adjustment resulted in a mean reprojection error of 0.55 pixels for the ground control points, confirming the geometric reliability of the imagery.

After we acquired the multispectral remote sensing image of the study area, the study further interpreted the land use/cover data to obtain spatial distribution data of rice. Based on the object-oriented concept within the eCognition software, we segmented the image using various scales, and ultimately the optimal segment scale of 1000 was used to accurately outline the feature boundaries of different land covers. Subsequently, five categories were established through visual interpretation including rice, buildings, rivers, roads, and vegetables. After selecting samples of each category, we used the nearest neighbor classification method to classify the image. In this approach, the classification was performed in the feature space using the minimum Euclidean distance criterion. The number of nearest

Table 1 Band details of the UAV multispectral image data

Band number	Band name	Central wavelength (nm)	Wavelength range (nm)
1	Blue	475	465–485
2	Green	560	550–570
3	Red	668	663–673
4	Red edge	717	712–722
5	NIR	840	820–860

neighbors (k) was set to 5, which is a commonly used value that balances sensitivity and robustness in classification tasks. The classification results were shown in Fig. 1c.

Experimental method

The complete technical route is shown in Fig. 2. This study processed the collected UAV multispectral image data and rice LAI data to construct a data set consisting of a modeling set (70%) and a validation set (30%) randomly. Based on the modeling set, a series of empirical and machine learning models were established, and these models were subsequently compared and validated using the validation set. Ultimately, the best-performing model was used for three periods of spatial LAI mapping.

Calculation methods of vegetation indices

The vegetation indices derived from the multi-spectral reflectances generally exhibited strong correlations with LAI (Liang et al., 2020; Parida et al., 2024). This study used five classic vegetation indices for analysis, namely NDVI, NGRDI, NDRE, RERVI and EVI. The calculation formulas of such vegetation indices were shown in Table 2.

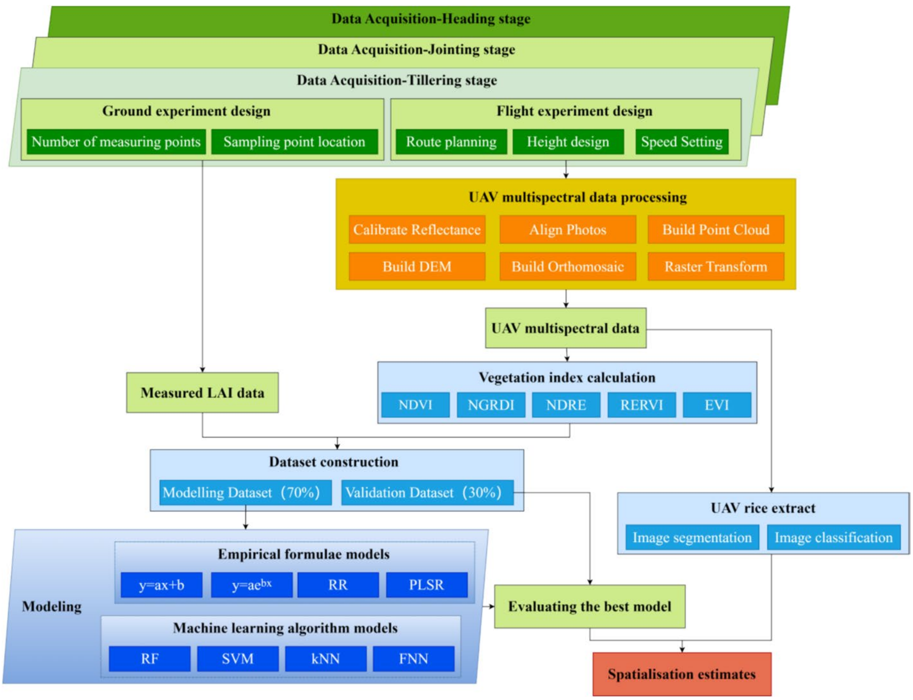

Fig. 2 Technology roadmap

Table 2 Calculation formula of vegetation index

Vegetation index	Name	Formula	Reference
Normalized Difference Vegetation Index	NDVI	$\frac{NIR-Red}{NIR+Red}$	Jiang et al., 2006
Normalized Green–Red Difference Index	NGRDI	$\frac{Green-Red}{Green+Red}$	Wang et al., 2023
Normalized Difference Red Edge Index	NDRE	$\frac{NIR-RedEdge}{NIR+RedEdge}$	Qiao et al., 2022
Red-Edge Ratio Vegetation Index	RERVI	$\frac{NIR}{RedEdge}$	Zhang et al., 2019
Enhanced Vegetation Index	EVI	$\frac{2.5(NIR-Red)}{NIR+6Red-7.5Blue+1}$	Potithep et al., 2013

Empirical algorithms

For the empirical model with single vegetation index as the independent variable, linear and nonlinear models were constructed:

$$\text{Linear model}: y = ax + b. \tag{1}$$

$$\text{Nonlinear model}: \; y = ae^{bx} . \tag{2}$$

Where *x* was the vegetation index calculated from the band reflectance, containing NDVI, NGRDI, NDRE, RERVI, and EVI, *y* was the measured rice LAI value, *a* and *b* were the coefficients of the formula in (1) and (2), respectively.

When used multiple vegetation indices as predictors, PLSR and RR are more suitable for modeling LAI compared to traditional multiple linear regression, as the latter need take the strong correlations that may exist among these predictors into account. PLSR is a multivariate statistical analysis method that effectively handles complex situations where the multiple independent variables are highly collinear. Its core concept is to select new orthogonal projection directions (principal components) that maximize the covariance between the dependent and independent variables on these projection axes, thereby constructing an efficient predictive model (Conforti et al., 2013). RR improves the least squares estimation method by introducing a penalty term, which results in a smaller mean square error and enhances the robustness of the model. The specific cost function is as follows:

$$\mathrm{J}\left(\theta\right) = \frac{1}{2\mathrm{m}}\left[\sum_{\mathrm{i}=1}^{\mathrm{m}}\left(\mathrm{h}_{\theta}\left(\mathrm{x}^{\mathrm{i}}\right) - \mathrm{y}^{\mathrm{i}}\right)^{2} + \lambda\sum_{\mathrm{j}=1}^{\mathrm{n}}\theta^{2}\right] \tag{3}$$

where *m* is the number of samples and *n* is the number of features. The function $\mathrm{h}_{\theta}(\mathrm{x})$ refers to the hypothesis function, which provides the model's estimation of the target variable based on the input features x. The cost function includes the penalty coefficient $\sum_{\mathrm{j}=1}^{\mathrm{n}}\theta^{2}$ and the ridge parameter λ, as well as the residual sum of squares is $\sum_{\mathrm{i}=1}^{\mathrm{m}}\left(\mathrm{h}_{\theta}\left(\mathrm{x}^{\mathrm{i}}\right) - \mathrm{y}^{\mathrm{i}}\right)^{2}$ from the original multiple linear regression (Ivanda et al., 2021; Ji et al., 2022). The use of the penalty term is aimed at regulating model complexity, preventing overfitting, and ensuring that the model maintains good performance even in the presence of multicollinearity.

Machine learning algorithms

Machine learning is a powerful tool capable of learning complex relationships between variables in high-dimensional spaces, demonstrating superior data adaptability through data mining (Jianya & Yansheng, 2022). Machine learning, especially deep learning, holds great potential in quantitative remote sensing studies. In this study, we compared the performances of four machine learning models including the RF, SVM, kNN, and FNN, respectively.

RF improves model accuracy and robustness by constructing multiple decision trees and integrating their prediction results. Specifically, in RF models, a subset of feature variables are randomly selected at each node split, and then the best split point is chosen among these variables to build each decision tree (Zhao et al., 2019). The key hyperparameters of the random forest model include the number of decision trees (n_estimators) and the number of features (max_features) considered when splitting nodes.

SVM is a supervised learning algorithm used for regression analysis. Especially for small sample problems, SVM can balance the complexity of the model and the number of training samples by adjusting the penalty term (Yuan et al., 2017). The regularization parameter C controls the model's tolerance for misclassification: a larger value of C makes the model more inclined to fit the training data. The kernel function typically chosen is the radial basis function, which can handle nonlinear relationships. Its parameter determines the decay rate of the similarity measure between samples, directly affecting the model's complexity and generalization capability.

The kNN adopts the "feature similarity principle". First, the distance between the input instance and the overall training sample is calculated, sorted according to the distance, and the k instances closest to the training data are selected to calculate the attributes of the input instance (Jiang et al., 2020). This study used the Manhattan distance, which represents the sum of the absolute values of the differences at each latitude in the multidimensional space.

FNN, a multi-layer neural network in deep learning, includes input, multiple hidden, and output layers. Data enters through the input layer, hidden nodes process it with weighted summation and activation functions, and the output layer produces results (Liu et al., 2022a, 2022b, 2022c; You et al., 2014). In this study, the FNN model takes five vegetation indices as input and LAI as output. The network includes an input layer, multiple hidden layers, and an output layer. Each hidden layer applies a linear transformation followed by *ReLU* activation and batch normalization. Residual connections add each hidden layer's input to its output. The model architecture is shown in Fig. 3.

Assuming the input feature is $x=[x_1, x_2, x_3, \dots x_n]$, the propagation of the input layer to the first hidden layer can be expressed as:

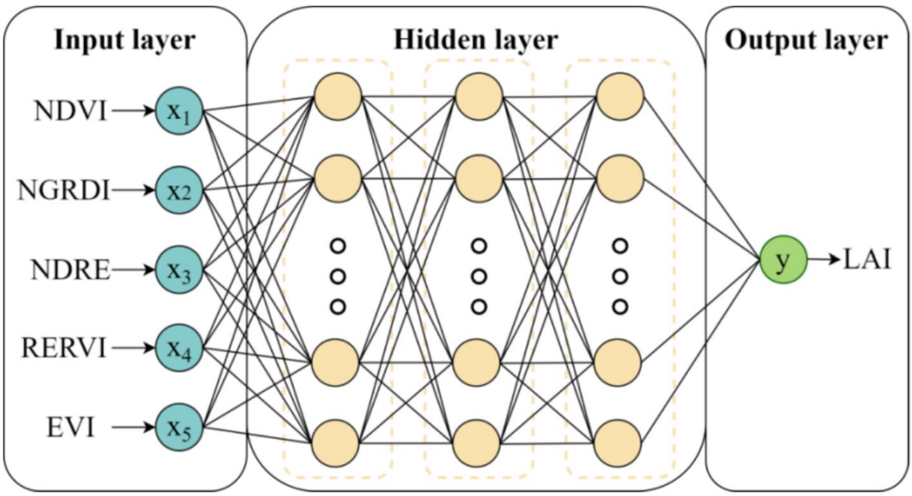

Fig. 3 FNN model structure

$$net_j = \sum_{i=1}^{n} w_{ij} x_i + b_j \tag{4}$$

where w_{ij} is the weight from the *i*—th node of the input layer to the *j*—th node of the hidden layer, and b_j is the bias of the *j*—th node in the hidden layer. The propagation from the *k*—th hidden layer to the (*k*+*1*)-th hidden layer can be expressed as:

$$net_j^{(k+1)} = \sum_{i=1}^{n_i} w_{ij}^k Z_i^k + b_j^{(k+1)} \tag{5}$$

where w_{ij}^k is the weight from the *i*—th node of the *k*—th layer to the *j*—th node of the (*k*+*1*)-th layer, and b_j^{k+1} is the bias of the *j*—th node in the (*k*+*1*)-th layer. Z_i^k represents the output of the *i*—th node in the *k*—th layer. This process introduces the *LeakyReLU* activation function:

$$Z_j^{(k+1)} = max\left(0.01net_j^{(k+1)}, net_j^{(k+1)}\right) \tag{6}$$

The function output its input when the input $net_j^{(k+1)}$ is greater than or equal to zero, and outputs 0.01 times $net_j^{(k+1)}$ when it is less than zero, which can effectively address the issue of vanishing gradients. Propagation from the hidden layer to the final output layer is expressed as:

$$y = f_p\left(\sum_{j=1}^{m} v_j Z_j\right) \tag{7}$$

where, v_j is the weight from the *j*—th node of the hidden layer to the output layer, and Z_j is the output of the *j*—th node of the hidden layer, $f_p(x) = x$ is a linear activation function (Fang et al., 2023). During the training process, the Mean Squared Error (MSE) is used as the loss function to calculate the prediction differences, with the formula being:

$$MSE = \frac{\sum_1^n (y_i - y_i')^2}{n} \tag{8}$$

where y_i is the measured LAI, y_i' is the predicted LAI, *n* is the total number of samples.

Model establishment and verification

This study constructed multiple models as shown in Table 3. Linear models were comprised of LAI-NDVI$_{\text{linear}}$, LAI-NGRDI$_{\text{linear}}$, LAI-NDRE$_{\text{linear}}$, LAI-RERVI$_{\text{linear}}$, LAI-EVI$_{\text{linear}}$, and nonlinear models included LAI-NDVI$_{\text{non-linear}}$, LAI-NGRDI$_{\text{non-linear}}$, LAI-NDRE$_{\text{non-linear}}$, LAI-RERVI$_{\text{non-linear}}$, LAI-EVI$_{\text{non-linear}}$. Meanwhile, the empirical models like LAI$_{\text{PLSR}}$, LAI$_{\text{RR}}$ and the machine learning models like LAI$_{\text{SVM}}$, LAI$_{\text{RF}}$, LAI$_{\text{kNN}}$, LAI$_{\text{FNN}}$ were developed based on multiple vegetation indices.

Table 3 Models developed in this study

Model name	Model input	Algorithm	Type
LAI-$NDVI_{linear}$	NDVI	$y=ax+b$	Empirical model
LAI-$NGRDI_{linear}$	NGRDI		
LAI-$NDRE_{linear}$	NDRE		
LAI-$RERVI_{linear}$	RERVI		
LAI-EVI_{linear}	EVI		
LAI-$NDVI_{non\text{-}linear}$	NDVI	$y=a * e^{bx}$	
LAI-$NGRDI_{non\text{-}linear}$	NGRDI		
LAI-$NDRE_{non\text{-}linear}$	NDRE		
LAI-$RERVI_{non\text{-}linear}$	RERVI		
LAI-$EVI_{non\text{-}linea}$	EVI		
LAI_{PLSR}	NDVI, NGRDI, NDRE, RERVI,EVI	PLSR	
LAI_{RR}		RR	
LAI_{SVM}		SVM	Machine learning model
LAI_{RF}		RF	
LAI_{kNN}		kNN	
LAI_{FNN}		FNN	

During model development, linear and nonlinear models based on single vegetation index were directly fitted using the 70% modeling set. Meanwhile, for models requiring internal parameter optimization, including PLSR, RR, SVM, RF, kNN, and FNN, the *fivefold* cross validation combined with *GridSearchCV* was conducted solely within the same 70% modeling set to determine the optimal structural parameters for each algorithm. The tuned parameters were then summarized, while any parameters not explicitly listed were retained at their default settings. LAI_{SVM}: Radial Basis Function (RBF) was selected as the kernel function, with a gamma value of 0.001 and a regularization parameter C of 10. LAI_{RF}: The number of decision trees was set to 100. The minimum number of samples required to be at a leaf node was 4, and the minimum number of samples required to split an internal node was 6. LAI_{kNN}: The number of nearest neighbors (n_neighbors) was set to 10. The distance metric used was Euclidean and the neighbors were weighted according to distance. LAI_{FNN}: The model was configured with one input layer, three hidden layers, and one output layer. Each hidden layer contained 128 neurons. For the LAI_{FNN} model, the loss function during training was used to quantify the prediction discrepancy. As shown in Fig. 4, the model did not converge when the learning rate was set to 10^{-5}. In contrast, with the other three learning rate settings, the model converged quickly and the loss became stable. When the learning rate was set to 10^{-3}, the loss value stabilized after about 10 epochs and reached the lowest level during training. Therefore, setting the learning rate to 10^{-5} and training for 50 epochs yielded the best performance.

During the model evaluation phase, both the coefficient of determination (R^2) and the root mean square error (RMSE) were used to assess the performance of all LAI inversion models, including linear and non-linear models based on single vegetation index, and empirical and machine learning models based on multiple vegetation indices, on the 30% validation set. R^2 is mainly used to measure the fitting effect of the model, and its value ranges from 0 to 1. RMSE is mainly used to measure the prediction error of the model. Generally, a large R^2 with a small RMSE corresponds to a higher prediction accuracy of the model. R^2 and RMSE are calculated as below:

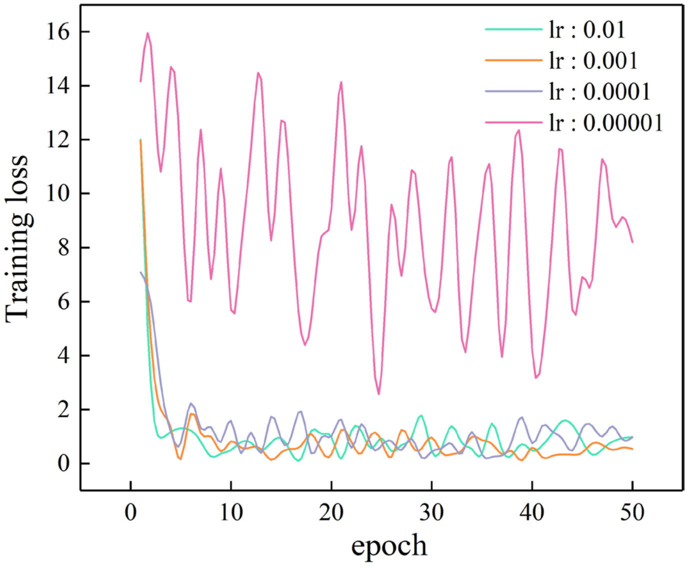

Fig. 4 Training loss curve of LAI_{FNN} under different learning rates

$$R^2 = 1 - \frac{\sum_1^n (y_i - y_i')^2}{\sum_1^n (y_i - \overline{y})^2} \tag{9}$$

$$RMSE = \sqrt{\frac{\sum_1^n (y_i - y_i')^2}{n}} \tag{10}$$

where y_i is the measured LAI, y_i' is the predicted LAI, $\overline{y}$ is the mean of the measured LAI, and n is the total number of samples in (9) and (10), respectively.

Feature importance analysis method

After identifying the best-performing model, to quantitatively evaluate the contribution of each input feature (i.e., the vegetation indices in this study) to the predictions of the optimal model, we employed the SHAP method for model interpretability analysis. SHAP is a model-agnostic interpretation framework based on Shapley value theory from cooperative game theory, providing a unified and equitable quantitative measure of each feature's contribution to model predictions (Wang et al., 2024). The core concept involves calculating the average marginal contribution of a feature across all possible feature combinations to assess its individual importance. In the specific calculation procedure, we utilized all samples from the validation set and applied the Kernel SHAP algorithm to estimate the SHAP value of each vegetation index for LAI prediction. To comprehensively assess the overall importance of each feature, we further computed its global mean absolute SHAP value. This metric reflects the average intensity of each feature's impact on the model predictions, with the calculation formula as follows:

$$mean(SHAP_j) = \frac{1}{n}\sum_{i=1}^{n}|\phi_j^{(i)}| \tag{11}$$

where $\phi_j^{(i)}$ denotes the SHAP value of the *j*—th feature for the *i*—th sample, and *n* represents the number of samples in the validation set.

Results and analyses

Linear and non-linear models based on single vegetation index

Based on the data from the training set, this study constructed the linear and nonlinear models based on single vegetation index including NDVI, NGRDI, NDRE, RERVI and EVI for LAI estimation, respectively. These models were then evaluated using the validation set, as presented in Table 4 and Fig. 5.

Specifically, EVI consistently demonstrated superior LAI estimation capability compared to the other four vegetation indices under both linear and nonlinear modeling frameworks. Notably, the LAI-EVI$_{\text{non-linear}}$ (R^2 = 0.756, RMSE = 0.680) model achieved the highest R^2 and the lowest RMSE among all single-index models, highlighting its robust performance across growth stages. The corresponding linear LAI-EVI$_{\text{linear}}$ model also performed well, with R^2 and RMSE of 0.676 and 0.782, respectively. By contrast, NDVI and NDRE yielded moderate estimation accuracy, with their linear models attaining R^2 values of 0.496 and 0.467, and RMSE values of 0.977 and 1.004, respectively. RERVI and NGRDI exhibited relatively weaker performance; for example, the LAI-NGRDI$_{\text{linear}}$ model achieved an R^2 of only 0.311 and an RMSE of 1.142, while the nonlinear LAI-RERVI$_{\text{non-linear}}$ model displayed the highest prediction error (RMSE = 1.347) among all models.

Comparing linear and nonlinear model forms reveals that for NDVI, NGRDI, NDRE, and RERVI, the linear models generally outperformed their nonlinear counterparts in terms of R^2, with differences in both R^2 and RMSE consistently below 0.1. This suggests that, under the observed conditions, the relationship between these indices and LAI is essentially linear. However, EVI exhibited a distinct pattern: its nonlinear model improved R^2 by 0.08 and reduced RMSE by 0.102 compared to the linear version, indicating a more pronounced nonlinear response that better captures LAI dynamics, especially under higher canopy cover conditions. The scatterplots between measured and predicted LAI (Fig. 5) further corrobo-

Table 4 Empirical models based on single vegetation index including NDVI, NGRDI, NDRE, RERVI and EVI

Vegetation index	Relation formula	R^2	RMSE
NDVI	$y = 5.111x - 0.851$	0.496	0.977
	$y = 0.607e^{2.012x}$	0.487	0.986
NGRDI	$y = 6.036x + 1.308$	0.311	1.142
	$y = 1.803e^{1.686x}$	0.279	1.168
NDRE	$y = 6.768x + 0.039$	0.467	1.004
	$y = 0.916e^{2.513x}$	0.407	1.121
RERVI	$y = 1.088x - 0.163$	0.339	1.119
	$y = 1.079e^{0.330x}$	0.288	1.347
EVI	$y = 7.975x - 0.889$	0.676	0.782
	$y = 0.664e^{2.810x}$	0.756	0.680

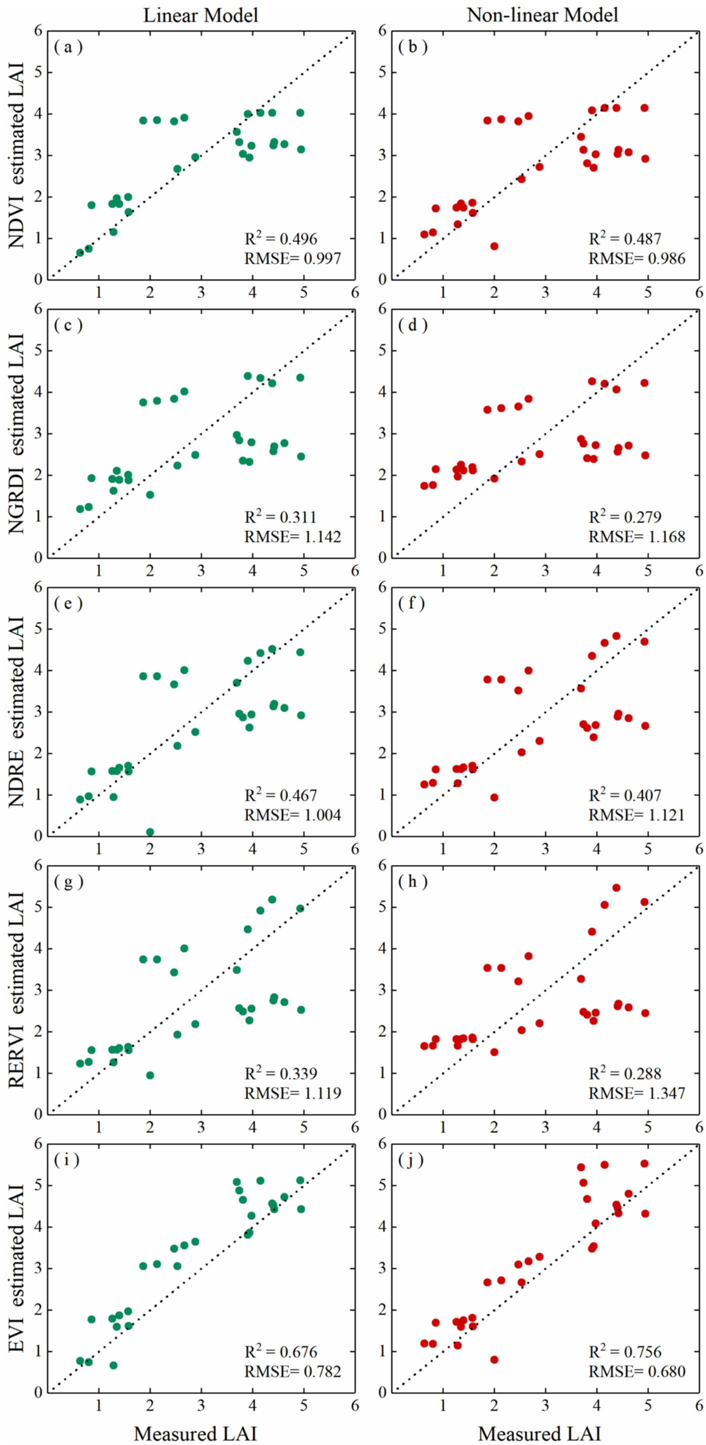

Fig. 5 The scatter plots between measured LAI and predicted LAI by the linear (**a**: NDVI; **c**: NGRDI; **e**: NDRE; **g**: RERVI; **i**: EVI) and non-linear (**b**: NDVI; **d**: NGRDI; **f**: NDRE; **h**: RERVI; **j**: EVI) models in Table 4

rate these findings. Predictions from both EVI models (Fig. 5i, j) clustered most tightly around the 1:1 line, with minimal bias across the LAI range. In comparison, predictions from NDVI-based models (Fig. 5a, b) tended to underestimate LAI at higher values, a pattern consistent with known spectral saturation effects. Predictions from RERVI and NGRDI models (Fig. 5g, h, c, d) showed greater scatter, particularly within the special LAI range (1.5—3.0), reflecting the lower stability and sensitivity of these indices.

In summary, EVI demonstrated its effectiveness as the most capable single vegetation index for LAI estimation, with its nonlinear form achieving the best overall performance. While NDVI and NDRE provided moderate accuracy, and RERVI and NGRDI exhibited weaker results, the linear models of all indices retained valuable information that could support the development of more robust multi-index fusion strategies in subsequent machine-learning approaches.

Empirical and machine learning models based on multiple vegetation indices

The study also developed the empirical models including the LAI_{PLSR} and LAI_{RR}, and the machine learning models including LAI_{SVM}, LAI_{RF}, LAI_{kNN} and LAI_{FNN}, as illustrated in Table 5 and Fig. 6.

The LAI_{RR} and LAI_{PLSR} models achieved R^2 of 0.705 and 0.698, and RMSE of 0.747 and 0.756, respectively, as detailed in Table 5 and Fig. 6a, b. Although the performance difference between these two linear methods was minor, both significantly outperformed all single-index models except LAI-$EVI_{non\text{-}linear}$, which attained an R^2 of 0.756 and an RMSE of 0.680, according to Table 4.

The shift from empirical models to machine learning models led to substantially improved LAI estimation accuracy. All machine learning algorithms, including LAI_{SVM}, LAI_{RF}, LAI_{kNN} and LAI_{FNN}, outperformed the multi-index empirical models. Among them, the LAI_{FNN} model achieved the highest overall performance with an R^2 of 0.821 and an RMSE of 0.583, as shown in Fig. 6f. The LAI_{kNN} model also performed strongly, with an R^2 of 0.807 and an RMSE of 0.604. LAI_{SVM} and LAI_{RF} delivered solid but comparatively lower results, achieving R^2 values of 0.773 and 0.778 and RMSE values of 0.655 and 0.648, respectively.

Upon identifying LAI_{FNN} as the optimal model, we performed a SHAP analysis to quantify feature importance. The mean absolute SHAP values (Fig. 7) ranked the vegetation indices as follows: EVI (0.526), RERVI (0.263), NGRDI (0.256), NDVI (0.224), and NDRE (0.197). EVI was the most dominant contributor, accounting for approximately 35.2% of the total importance, underscoring its critical role in LAI estimation across rice growth stages. The remaining four indices, while less influential, still provided substantial collective contributions, representing about 64.8% of the total importance.

Table 5 Empirical and machine learning models based on multiple vegetation indices including NDVI, NGRDI, NDRE, RERVI and EVI

Model input	Model algorithm	R^2	RMSE
NDVI, NGRDI, NDRE, RERVI, EVI	PLSR	0.698	0.756
	RR	0.705	0.747
	SVM	0.773	0.655
	RF	0.778	0.648
	kNN	0.807	0.604
	FNN	0.821	0.583

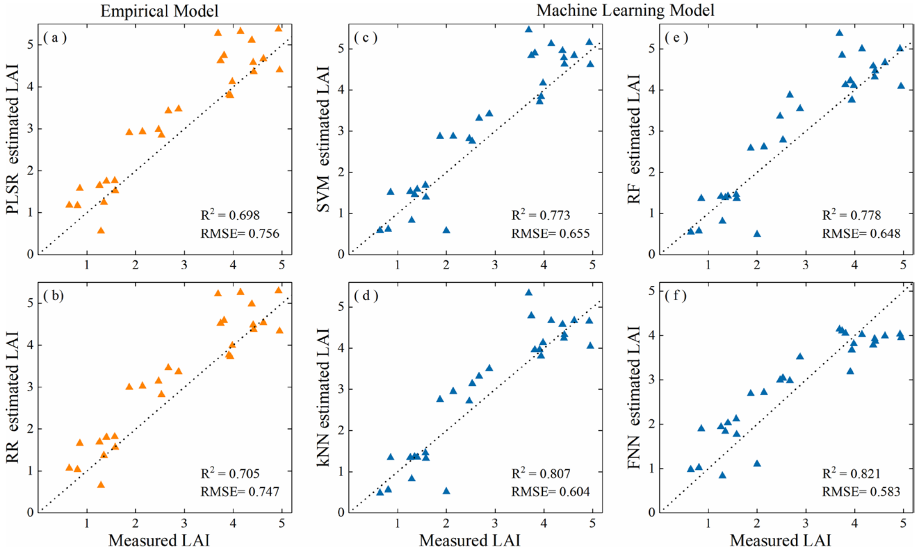

Fig. 6 The scatter plots between measured LAI and predicted LAI by the empirical (**a**: PLSR; **b**: RR) and machine learning (**c**: SVM; **d**: kNN; **e**: RF; **f**: FNN) models based on multiple vegetation indices as shown in Table 5

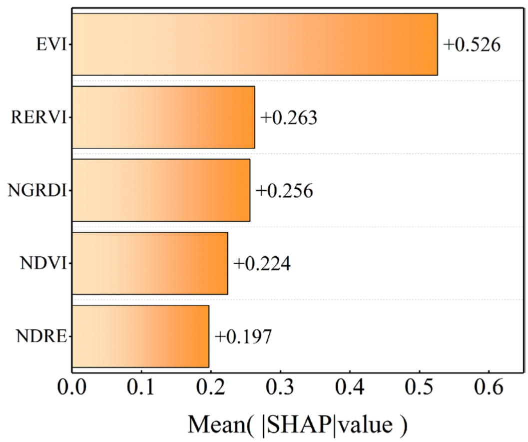

Fig. 7 Feature importance measured by mean absolute SHAP values (mean(|SHAP|)) for NDVI, NGRDI, NDRE, RERVI, and EVI in the LAI_{FNN} model

Model application for spatial estimation

The LAI_{FNN} model that demonstrated optimal performance on the 30% validation set, as evaluated by the highest R^2 and lowest RMSE metrics, was subsequently employed to map the spatial patterns of rice LAI across the three critical growth stages: tillering, jointing, and heading (Fig. 8). The associated histograms of LAI distribution for each period were shown in Fig. 9. Given the differences in management practices among different plots, the entire study area were roughly divided into three distinct parts including the upper, middle and lower sub-regions.

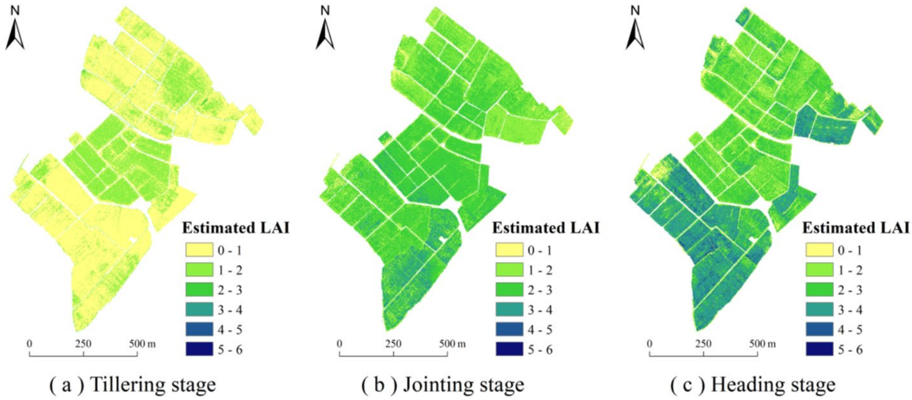

Fig. 8 Spatial inversion results of rice LAI across the critical growth stages including the tillering stage (**a**), jointing stage (**b**) and heading stage (**c**)

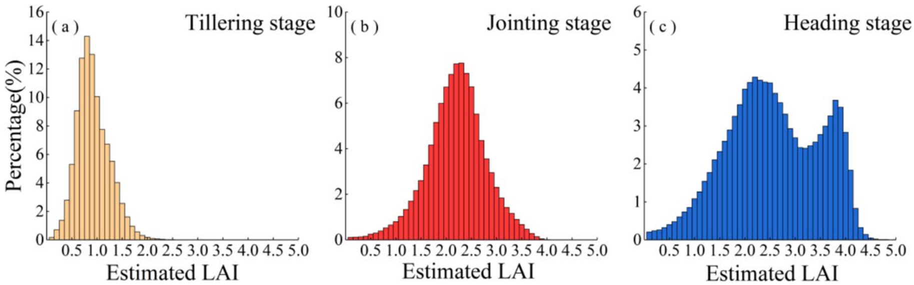

Fig. 9 Histogram of LAI values distribution of rice in different growth stages (**a**: tillering stage; **b**: jointing stage; **c**: heading stage)

During the tillering stage of rice in Fig. 9a, in general, the LAI values were relatively low with the regional mean LAI by 0.87. The proportion of pixels with LAI within one standard deviation ranging from 0.54 to 1.2 occupied by about 70.6% of the total area. Meanwhile, the LAI values of the central plot exhibited higher values, while the LAI values of the upper and lower plots were relatively lower. After entering the jointing stage of rice in Fig. 9b, the regional mean LAI value was 2.14 with the spatial differences tending to narrow. The proportion of pixels with LAI within one standard deviation between 1.54 and 2.74 occupied by about 72.3% of the total area. When rice reached the heading stage in Fig. 9c, the LAI values peaked by about 2.48, with the proportion of pixels within one standard deviation occupying by about 64.1%. Larger LAI values appeared in the lower plot than the upper and middle plots.

Discussion

Monitoring the variability in rice LAI is crucial for evaluating crop growth status and devising scientific farmland management strategies. Previous studies often used the empirical models to monitor crop LAI by integrating ground measured data and associated remote sensing data (Ma et al., 2022; Pan et al., 2023; Zu et al., 2024), whereas with the rapid advancement of artificial intelligence technologies in recent years, machine learning algorithms have been increasingly applied in the domain (Alfred et al., 2021; Lin et al., 2022a, 2022b). Nevertheless, the potential for rice LAI estimation throughout the growth period, especially for the deep learning methods, still requires further exploration. Given the great potential of machine learning in the field of data mining, this study compared a variety of machine learning and empirical models to provide support for further coupling machine learning technology with agriculture remote sensing.

This study compared the performance differences of linear and nonlinear models based on single vegetation index, and found that except the EVI, all other vegetation indices showed relatively better LAI estimates by the linear models (Table 4, Fig. 5). This difference may be related to the saturation characteristics of different vegetation index. As rice grows, vegetation indices tend to reach saturation, reducing their sensitivity to further changes in LAI (Din et al., 2017; Liu et al., 2022a, 2022b, 2022c). However, crops cannot grow indefinitely; typically, LAI ceases to increase significantly after the late jointing stage. Therefore, the nonlinear models often demonstrate stronger fitting capabilities. In this study, the LAI-$EVI_{non\text{-}linear}$ yielded better LAI estimation performance compared to LAI-EVI_{linear}, which confirmed this point. The EVI-based model achieved the highest accuracy, likely benefiting from the inclusion of the blue band (Son et al., 2014; Yao et al., 2017). Relative to the red band, the blue band is markedly more sensitive to atmospheric aerosol scattering, sharpening the contrast between the vegetation signal and atmospheric noise and thereby stabilising the index under variable atmospheric conditions. Moreover, during rice's early growth, when the canopy is incomplete and the background is dominated by water and bare soil, EVI suppresses this background contamination more effectively than other indices. The relatively poor fitting performance of the NDVI and NGRDI models stems from their reliance on the spectral response mechanisms of the visible bands (red and green). As the canopy approaches closure, their response to 'green area' tends to saturate, making it difficult to effectively detect further increases in canopy thickness, as quantified by LAI. In contrast, NDRE and RERVI utilize the red-edge region, which is sensitive to leaf biochemical components, while EVI effectively suppresses background interference through multispectral combination. These characteristics enable them to better reflect the vertical structure and overall biophysical state of the canopy, thus demonstrating more robust modeling capability in datasets covering multiple growth stages with a wide dynamic range of LAI (Gao et al., 2023; Lv et al., 2024).

Furthermore, Hang et al. (2021) utilized the UAV multispectral data and the multiple stepwise regression model to monitor rice LAI. The model also achieved higher accuracy, but the data used only covered two growth stages including the jointing and heading stages. Except the machine learning models, our study also evaluated the PLSR and RR-based empirical models for rice LAI estimates, and all machine learning models were found with better performance (Table 5, Fig. 6), which once again emphasized the significant role of machine learning in quantitative remote sensing research. It is noteworthy that Liu et al.

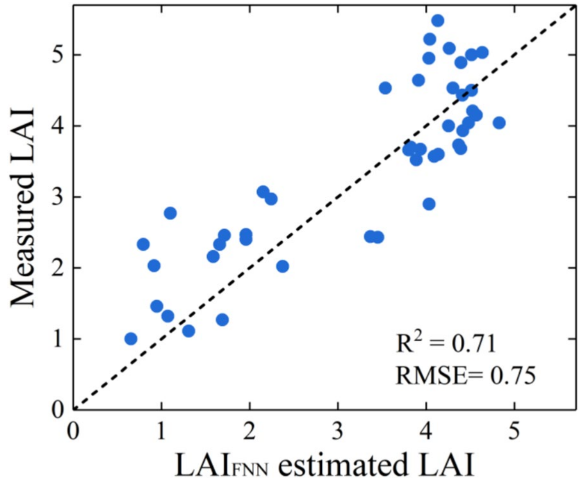

Fig. 10 Scatter plots between the independent measured LAI with predictions from the LAI_{FNN} model

(2021) trained deep learning models using large-scale observational data spanning multiple growing seasons and diverse crops, emphasizing that model performance heavily relies on sufficient sample support. Meanwhile, Li et al., (2025a, 2025b) developed a unified deep learning framework for the entire rice growth cycle, achieving high accuracy through dense ground-sampling designs under a tightly controlled experimental environment. Although the proposed LAI_{FNN} model slightly lags behind the aforementioned studies in absolute accuracy, it achieved a more practical balance among predictive accuracy, computational efficiency, and generalization capability, thereby offering a feasible approach for dynamic LAI monitoring under resource-constrained conditions. While this study had a relatively small sample size, which may reduce accuracy compared to prior work, its dataset was more representative, spatially balanced, and transferable. Although the LAI_{FNN} model achieved the highest predictive accuracy, it is particularly necessary to examine the trade-off between its performance gain and increased model complexity against the baseline of the LAI-$EVI_{non\text{-}linear}$ model. The LAI-$EVI_{non\text{-}linear}$ model may offer advantages in practical applications due to its low computational resource requirements, ease of deployment on low-cost devices, and the interpretability of its model parameters. Conversely, for large-scale monitoring programs or research contexts pursuing predictive accuracy, the additional accuracy gain provided by the LAI_{FNN} model may justify its complexity. In summary, the practical selection of a model should not pursue a single standard of optimality, but should be based on specific application requirements, making a comprehensive trade-off among factors such as accuracy, interpretability, computational efficiency, and robustness under limited data.

To further evaluate the generalization capability and robustness of the LAI_{FNN} model, we conducted an independent validation experiment. In 2025, new ground-based LAI measurements and UAV multispectral images were collected during two key rice growth stages in the study area: the tillering stage (May 19, 2025) and the jointing stage (June 17, 2025), resulting in a total of 46 independent samples. It is important to note that this 2025 campaign did not include the heading stage, a critical reproductive phase where panicle emergence can substantially alter canopy structure and spectral responses. As shown in Fig. 10, the validation results showed an R^2 of 0.71 and an RMSE of 0.75. These findings indicate that the LAI_{FNN} model can effectively adapt to data variations across different years and vegetative growth stages while maintaining stable predictive performance under conditions of temporal continuity and environmental variability during the pre-reproductive phase.

Moreover, the superior performance of the LAI_{FNN} model may be partially attributed to architectural enhancements such as residual connections and batch normalization (Baz et al., 2024), which were known to facilitate training stability and mitigate gradient degradation in deep networks. We hypothesized that these components contribute to the model's improved generalization across diverse growth stages. However, without dedicated ablation studies isolating the effect of each component, it remained a plausible but unverified explanation. Consequently, while the model was trained on data covering the full growth cycle, its cross-year transferability to the reproductive stage (specifically the heading stage) remains to be verified with future multi-year data encompassing this critical phase.

Nevertheless, UAV-based remote sensing also involved practical constraints that affected its operational scalability. Effective deployment relied on trained operators, suitable weather conditions such as low wind speeds and no precipitation, and compliance with local aviation regulations. Additionally, raw UAV imagery generally required substantial post-processing, including radiometric calibration, image stitching, orthorectification, and vegetation index computation, all of which incur significant computational costs, processing time, and technical expertise (Li et al., 2025a, 2025b). These factors may limit the feasibility of UAV systems in resource-limited or large-scale agricultural settings, highlighting the need for streamlined, automated, and robust analytical workflows. A limitation of this study is that the adopted FNN architecture contains a large number of trainable parameters, far exceeding the number of available training samples, which poses a potential risk of overfitting. Sensitivity analysis showed that when the number of hidden layer neurons was reduced from 128 to 64, 32, 16, and 8, the R^2 values on the validation set exhibited varying degrees of decline. More importantly, the model maintained stable predictive performance in an independent cross-year validation using 2025 data ($R^2 = 0.71$, RMSE = 0.75), demonstrating its good generalization ability during the vegetative stages. Furthermore, overfitting during training was effectively controlled through the introduction of regularization strategies such as batch normalization and early stopping. Nevertheless, we acknowledge that the high parameter-to-sample ratio remains a theoretical constraint, implying that the model's stability may be sensitive to data variations not present in the current dataset. Future work will focus on collecting larger datasets to achieve a more statistically balanced model architecture.

Conclusions

Based on the UAV multi-spectral remote sensing data collected during multiple critical growth stages of rice in Zhejiang Province, China, this study examined the performance differences among the linear and non-linear models based on single vegetation index, and the empirical and machine learning models based on multiple vegetation indices, for LAI estimation. We mainly found that among these empirical models, the PLSR and RR-based LAI estimates based on multiple vegetation indices were not the best, whereas the LAI-$EVI_{non\text{-}linear}$ model performed the best with R^2 of 0.756 and RMSE of 0.680, respectively. In comparison, all models built based on the machine learning algorithms outperformed the empirical models in terms of prediction accuracy and data fitting. Meanwhile, the deep learning-based LAI_{FNN} model exhibited the highest accuracy, with R^2 of 0.821 and RMSE of 0.583, respectively. The SHAP-based feature importance analysis implied that EVI contributed most to the LAI_{FNN} model, accounting for about 35.2% of the total importance. The spatial mapping of rice LAI also captured the differences in management strategy. All these analyses implied the great potential of combining UAV remote sensing data with machine learning technology in the field of precision agriculture monitoring.

Acknowledgements This work was supported by the project of Strategic Science and Technology Innovation Cooperation from National Key Research and Development Program (2026YFE0212200).

Data availability All data can be accessed via the corresponding author upon request.

Declarations

Conflict of interest The authors declare that they have no known competing financial interests or personal relationships that could have appeared to influence the work reported in this paper.

References

Ahmad, R., Yang, B., Ettlin, G., Berger, A., & Rodríguez-Bocca, P. (2023). A machine-learning based ConvLSTM architecture for NDVI forecasting. *International Transactions in Operational Research, 30*(4), 2025–2048. https://doi.org/10.1111/itor.12887

Alfred, R., Obit, J. H., Chin, C. P. Y., Haviluddin, H., & Lim, Y. (2021). Towards paddy rice smart farming: A review on big data, machine learning, and rice production tasks. *IEEE Access, 9*, 50358–50380. https://doi.org/10.1109/ACCESS.2021.3069449

Bajocco, S., Ginaldi, F., Savian, F., Morelli, D., Scaglione, M., Fanchini, D., Raparelli, E., & Bregaglio, S. U. M. (2022). On the use of NDVI to estimate LAI in field crops: Implementing a conversion equation library. *Remote Sensing, 14*(15), Article 3554. https://doi.org/10.3390/rs14153554

Bandumula, N. (2018). Rice production in Asia: Key to global food security. *Proceedings of the National Academy of Sciences, India Section B: Biological Sciences, 88*(4), 1323–1328. https://doi.org/10.1007/s40011-017-0867-7

Barrero, O., & Perdomo, S. A. (2018). RGB and multispectral UAV image fusion for Gramineae weed detection in rice fields. *Precision Agriculture, 19*(5), 809–822. https://doi.org/10.1007/s11119-017-9558-x

Baz, A., Logeshwaran, J., Natarajan, Y., & Patel, S. K. (2024). Enhancing mobility management in 5G networks using deep residual LSTM model. *Applied Soft Computing, 165*, Article 112103. https://doi.org/10.1016/j.asoc.2024.112103

Chen, Y., Ding, Z., Yu, P., Yang, H., Song, L., Fan, L., Han, X., Ma, M., & Tang, X. (2022). Quantifying the variability in water use efficiency from the canopy to ecosystem scale across main croplands. *Agricultural Water Management, 262*, Article 107427. https://doi.org/10.1016/j.agwat.2021.107427

Chen, Y., Wang, Y., Wu, C., Jardim, A. M. D. R. F., Fang, M., Yao, L., Rosa Ferraz Jardim, AMd., Liu, G., Xu, Q., Chen, L., & Tang, X. (2025). Drought-induced stress on rainfed and irrigated agriculture: Insights from multi-source satellite-derived ecological indicators. *Agricultural Water Management, 307*, Article 109249. https://doi.org/10.1016/j.agwat.2024.109249

Cheng, Q., Ding, F., Xu, H., Guo, S., Li, Z., & Chen, Z. (2024). Quantifying corn LAI using machine learning and UAV multispectral imaging. *Precision Agriculture, 25*(4), 1777–1799. https://doi.org/10.1007/s11119-024-10134-z

Colombo, R., Bellingeri, D., Fasolini, D., & Marino, C. M. (2003). Retrieval of leaf area index in different vegetation types using high resolution satellite data. *Remote Sensing of Environment, 86*(1), 120–131. https://doi.org/10.1016/S0034-4257(03)00094-4

Conforti, M., Buttafuoco, G., Leone, A. P., Aucelli, P. P., Robustelli, G., & Scarciglia, F. (2013). Studying the relationship between water-induced soil erosion and soil organic matter using Vis–NIR spectroscopy and geomorphological analysis: A case study in southern Italy. *CATENA, 110*, 44–58. https://doi.org/10.1016/j.catena.2013.06.013

Dhakar, R., Sehgal, V. K., Chakraborty, D., Sahoo, R. N., & Mukherjee, J. (2021). Field scale wheat LAI retrieval from multispectral Sentinel 2A-MSI and LandSat 8-OLI imagery: Effect of atmospheric correction, image resolutions and inversion techniques. *Geocarto International, 36*(18), 2044–2064. https://doi.org/10.1080/10106049.2019.1687591

Din, M., Zheng, W., Rashid, M., Wang, S., & Shi, Z. (2017). Evaluating hyperspectral vegetation indices for leaf area index estimation of *Oryza sativa* L. at diverse phenological stages. *Frontiers in Plant Science, 8*, Article 820. https://doi.org/10.3389/fpls.2017.00820

Fang, H., Li, W., Wei, S., & Jiang, C. (2014). Seasonal variation of leaf area index (LAI) over paddy rice fields in NE China: Intercomparison of destructive sampling, LAI-2200, digital hemispherical photography (DHP), and AccuPAR methods. *Agricultural and Forest Meteorology, 198*, 126–141. https://doi.org/10.1016/j.agrformet.2014.08.005

Fang, T., Zheng, C., & Wang, D. (2023). Forecasting the crude oil prices with an EMD-ISBM-FNN model. *Energy, 263*, Article 125407. https://doi.org/10.1016/j.energy.2022.125407

Fei, S., Hassan, M. A., Xiao, Y., Su, X., Chen, Z., Cheng, Q., & Ma, Y. (2023). UAV-based multi-sensor data fusion and machine learning algorithm for yield prediction in wheat. *Precision Agriculture, 24*(1), 187–212. https://doi.org/10.1007/s11119-022-09938-8

Gao, L., Yang, G., Yu, H., Xu, B., Zhao, X., Dong, J., & Ma, Y. (2016). Retrieving winter wheat leaf area index based on unmanned aerial vehicle hyperspectral remote sensing. *Transactions of the Chinese Society of Agricultural Engineering, 32*(22), 113–120. https://doi.org/10.11975/j.issn.1002-6819.2016.22.016

Gao, S., Zhong, R., Yan, K., Ma, X., Chen, X., Pu, J., Qi, J., Yin, G., & Myneni, R. B. (2023). Evaluating the saturation effect of vegetation indices in forests using 3D radiative transfer simulations and satellite observations. *Remote Sensing of Environment, 295*, Article 113665. https://doi.org/10.1016/j.rse.2023.113665

Hammond, K., Kerry, R., Jensen, R. R., Spackman, R., Hulet, A., Hopkins, B. G., Yost, M. A., Hopkins, A. P., & Hansen, N. C. (2023). Assessing within-field variation in alfalfa leaf area index using UAV visible vegetation indices. *Agronomy, 13*(5), Article 1289. https://doi.org/10.3390/agronomy13051289

Han, L., Chen, Y., Wu, C., Yao, L., Wang, Y., Su, C., Li, X., da Rosa Ferraz Jardim, A. M., Freire da Silva, T. G., & Tang, X. (2025). Divergent drought-induced suppression on vegetation and associated feedbacks: Satellite-based observations in 2022 across the Yangtze River basin, China. *Journal of Hydrology, 661*, Article 133673. https://doi.org/10.1016/j.jhydrol.2025.133673

Hang, Y., Su, H., Yu, Z., Liu, H., Guan, H., & Kong, F. (2021). Estimation of rice leaf area index combining UAV spectrum, texture features and vegetation coverage. Transactions of the Chinese Society of Agricultural Engineering*, 37*(9), 64–71. https://doi.org/10.11975/j.issn.1002-6819.2021.09.008

Ivanda, A., Šerić, L., Bugarić, M., & Braović, M. (2021). Mapping chlorophyll-a concentrations in the Kaštela Bay and Brač Channel using ridge regression and Sentinel-2 satellite images. *Electronics, 10*(23), Article 3004. https://doi.org/10.3390/electronics10233004

Ji, S., Gu, C., Xi, X., Zhang, Z., Hong, Q., Huo, Z., Zhao, H., Zhang, R., Li, B., & Tan, C. (2022). Quantitative monitoring of leaf area index in rice based on hyperspectral feature bands and ridge regression algorithm. *Remote Sensing, 14*(12), Article 2777. https://doi.org/10.3390/rs14122777

Jiang, F., Smith, A. R., Kutia, M., Wang, G., Liu, H., & Sun, H. (2020). A modified KNN method for mapping the leaf area index in arid and semi-arid areas of China. *Remote Sensing, 12*(11), 1884. https://doi.org/10.3390/rs12111884

Jiang, H., Wei, X., Chen, Z., Zhu, M., Yao, Y., Zhang, X., & Jia, K. (2023). Influence of different soil reflectance schemes on the retrieval of vegetation LAI and FVC from PROSAIL in agriculture region. *Computers and Electronics in Agriculture, 212*, Article 108165. https://doi.org/10.1016/j.compag.2023.108165

Jiang, Z., Huete, A. R., Chen, J., Chen, Y., Li, J., Yan, G., & Zhang, X. (2006). Analysis of NDVI and scaled difference vegetation index retrievals of vegetation fraction. *Remote Sensing of Environment, 101*(3), 366–378. https://doi.org/10.1016/j.rse.2006.01.003

Jianya, G., & Yansheng, L. (2022). Can quantitative remote sensing and machine learning be integrated? *Earth Sciences, 47*(10), 3911–3912. https://doi.org/10.3799/dqkx.2022.861

Kang, Y., Özdoğan, M., Zipper, S. C., Román, M. O., Walker, J., Hong, S. Y., & Loheide, S. P. (2016). How universal is the relationship between remotely sensed vegetation indices and crop leaf area index? A global assessment. *Remote Sensing, 8*(7), 597. https://doi.org/10.3390/rs8070597

Kimm, H., Guan, K., Jiang, C., Peng, B., Gentry, L. F., Wilkin, S. C., & Luo, Y. (2020). Deriving high-spatiotemporal-resolution leaf area index for agroecosystems in the US Corn Belt using Planet Labs CubeSat and STAIR fusion data. *Remote Sensing of Environment, 239*, 111615. https://doi.org/10.1016/j.rse.2019.111615

Li, H., Li, Q., Yu, C., & Luo, S. (2025a). Unified estimation of rice canopy leaf area index over multiple periods based on UAV multispectral imagery and deep learning. *Plant Methods, 21*(1), 73. https://doi.org/10.1186/s13007-025-01398-1

Li, H., Yue, L., & Luo, S. (2025b). Estimating the full-period rice leaf area index using CNN-LSTM-Attention and multispectral images from unmanned aerial vehicles. *Frontiers in Plant Science, 16*, 1636967. https://doi.org/10.3389/fpls.2025.1636967

Li, S., Yuan, F., Ata-UI-Karim, S. T., Zheng, H., Cheng, T., Liu, X., & Cao, Q. (2019). Combining color indices and textures of UAV-based digital imagery for rice LAI estimation. *Remote Sensing, 11*(15), 1763. https://doi.org/10.3390/rs11151763

Liang, L., Huang, T., Di, L., Geng, D., Yan, J., Wang, S., & Kang, J. (2020). Influence of different bandwidths on LAI estimation using vegetation indices. *IEEE Journal of Selected Topics in Applied Earth Observations and Remote Sensing, 13*, 1494–1502. https://doi.org/10.1109/JSTARS.2020.2984608

Lin, H. I., Yu, Y. Y., Wen, F. I., & Liu, P. T. (2022a). Status of food security in East and Southeast Asia and challenges of climate change. *Climate, 10*(3), Article 40. https://doi.org/10.3390/cli10030040

Lin, Y. D., Liu, Z. Q., Hwang, R. H., Nguyen, V. L., Lin, P. C., & Lai, Y. C. (2022b). Machine learning with variational autoencoder for imbalanced datasets in intrusion detection. *IEEE Access, 10*, 15247–15260. https://doi.org/10.1109/ACCESS.2022.3149295

Liu, H., Jin, Y., Song, X., & Pei, Z. (2022a). Rate of penetration prediction method for ultra-deep wells based on LSTM–FNN. *Applied Sciences, 12*(15), Article 7731. https://doi.org/10.3390/app12157731

Liu, H., Su, X., Zhang, C., & An, H. (2022b). Landscape tree species recognition using RedEdge-MX: Suitability analysis of two different texture extraction forms under MLC and RF supervision. *Open Geosciences, 14*(1), 985–994. https://doi.org/10.1515/geo-2022-0416

Liu, S., Hu, Z., Han, J., Li, Y., & Zhou, T. (2022c). Predicting grain yield and protein content of winter wheat at different growth stages by hyperspectral data integrated with growth monitor index. *Computers and Electronics in Agriculture, 200*, Article 107235. https://doi.org/10.1016/j.compag.2022.107235

Liu, S., Jin, X., Nie, C., Wang, S., Yu, X., Cheng, M., Shao, M., Wang, Z., Tuohuti, N., Bai, Y., & Liu, Y. (2021). Estimating leaf area index using unmanned aerial vehicle data: Shallow vs. deep machine learning algorithms. *Plant Physiology, 187*(3), 1551–1576. https://doi.org/10.1093/plphys/kiab322

Luo, P., Liao, J., & Shen, G. (2020a). Combining spectral and texture features for estimating leaf area index and biomass of maize using Sentinel-1/2, and Landsat-8 data. *IEEE Access, 8*, 53614–53626. https://doi.org/10.1109/ACCESS.2020.2981492

Luo, Y., Zhang, Z., Li, Z., Chen, Y., Zhang, L., Cao, J., & Tao, F. (2020b). Identifying the spatiotemporal changes of annual harvesting areas for three staple crops in China by integrating multi-data sources. *Environmental Research Letters, 15*(7), Article 074003. https://doi.org/10.1088/1748-9326/ab80f0

Lv, F., Sun, K., Li, W., Miao, S., & Hu, X. (2024). Estimation of leaf area index across biomes and growth stages combining multiple vegetation indices. *Sensors, 24*(18), Article 6106. https://doi.org/10.3390/s24186106

Ma, J., Wang, L., & Chen, P. (2022). Comparing different methods for wheat LAI inversion based on hyperspectral data. *Agriculture, 12*(9), 1353. https://doi.org/10.3390/agriculture12091353

Nazir, A., Ullah, S., Saqib, Z. A., Abbas, A., Ali, A., Iqbal, M. S., Hussain, K., Shakir, M., Shah, M., & Butt, M. U. (2021). Estimation and forecasting of rice yield using phenology-based algorithm and linear regression model on Sentinel-II satellite data. *Agriculture, 11*(10), Article 1026. https://doi.org/10.3390/agriculture11101026

Pan, F., Guo, J., Miao, J., Xu, H., Tian, B., Gong, D., Zhao, J., & Lan, Y. (2023). Summer maize LAI retrieval based on multi-source remote sensing data. *International Journal of Agricultural and Biological Engineering, 16*(2), 179–186. https://doi.org/10.25165/j.ijabe.20231602.7285

Papapicco, D., Demo, N., Girfoglio, M., Stabile, G., & Rozza, G. (2022). The neural network shifted-proper orthogonal decomposition: A machine learning approach for non-linear reduction of hyperbolic equations. *Computer Methods in Applied Mechanics and Engineering, 392*, Article 114687. https://doi.org/10.1016/j.cma.2022.114687

Parida, P. K., Somasundaram, E., Krishnan, R., Radhamani, S., Sivakumar, U., Parameswari, E., Raja, R., Shri Rangasami, S. R., Sangeetha, S. P., & Gangai Selvi, R. (2024). Unmanned aerial vehicle-measured multispectral vegetation indices for predicting LAI, SPAD chlorophyll, and yield of maize. *Agriculture*. https://doi.org/10.3390/agriculture14071110

Potithep, S., Nagai, S., Nasahara, K. N., Muraoka, H., & Suzuki, R. (2013). Two separate periods of the LAI–VIs relationships using in situ measurements in a deciduous broadleaf forest. *Agricultural and Forest Meteorology, 169*, 148–155. https://doi.org/10.1016/j.agrformet.2012.09.003

Prabhakar, M., Gopinath, K. A., Ravi Kumar, N., Thirupathi, M., Sai Sravan, U., Srasvan Kumar, G., Samba Siva, G., Chandana, P., & Singh, V. K. (2024). Mapping leaf area index at various rice growth stages in Southern India using airborne hyperspectral remote sensing. *Remote Sensing, 16*(6), Article 954. https://doi.org/10.3390/rs16060954

Qiao, L., Zhao, R., Tang, W., An, L., Sun, H., Li, M., Wang, N., Liu, Y., & Liu, G. (2022). Estimating maize LAI by exploring deep features of vegetation index map from UAV multispectral images. *Field Crops Research, 289*, Article 108739. https://doi.org/10.1016/j.fcr.2022.108739

Raj, R., Walker, J. P., Pingale, R., Nandan, R., Naik, B., & Jagarlapudi, A. (2021). Leaf area index estimation using top-of-canopy airborne RGB images. *International Journal of Applied Earth Observation and Geoinformation, 96*, Article 102282. https://doi.org/10.1016/j.jag.2020.102282

Shaheen, S. M., Antoniadis, V., Shahid, M., Yang, Y., Abdelrahman, H., Zhang, T., Hassan, N. E. E., Bibi, I., Niazi, N. K., Younis, S. A., Almazroui, M., Tsang, Y. F., Sarmah, A. K., Kim, K.-H., & Rinklebe, J. (2022). Sustainable applications of rice feedstock in agro-environmental and construction sectors: A global perspective. *Renewable and Sustainable Energy Reviews, 153*, Article 111791. https://doi.org/10.1016/j.rser.2021.111791

Son, N. T., Chen, C. F., Chen, C. R., Minh, V. Q., & Trung, N. H. (2014). A comparative analysis of multitemporal MODIS EVI and NDVI data for large-scale rice yield estimation. *Agricultural and Forest Meteorology, 197*, 52–64. https://doi.org/10.1016/j.agrformet.2014.06.007

Sun, B., Li, Y., Huang, J., Cao, Z., & Peng, X. (2024). Impacts of variable illumination and image background on rice LAI estimation based on UAV RGB-derived color indices. *Applied Sciences, 14*(8), Article 3214. https://doi.org/10.3390/app14083214

Sun, Q., Jiao, Q., Chen, X., Xing, H., Huang, W., & Zhang, B. (2023). Machine learning algorithms for the retrieval of canopy chlorophyll content and leaf area index of crops using the PROSAIL-D model with the adjusted average leaf angle. *Remote Sensing, 15*(9), Article 2264. https://doi.org/10.3390/rs15092264

Sun, Y., Qin, Q., Ren, H., & Zhang, Y. (2021). Decameter cropland LAI/FPAR estimation from Sentinel-2 imagery using google earth engine. *IEEE Transactions on Geoscience and Remote Sensing, 60*, 1–14. https://doi.org/10.1109/TGRS.2021.3052254

Vishwakarma, S. K., Bhattarai, B., Kothari, K., & Pandey, A. (2025). Intercomparison of machine learning models for estimating leaf area index of rice using UAV-based multispectral imagery. *Physics and Chemistry of the Earth, Parts A/B/C*. https://doi.org/10.1016/j.pce.2025.103977

Wang, H., Liang, Q., Hancock, J. T., & Khoshgoftaar, T. M. (2024). Feature selection strategies: A comparative analysis of SHAP-value and importance-based methods. *Journal of Big Data, 11*(1), Article 44. https://doi.org/10.1186/s40537-024-00905-w

Wang, X., Yan, S., Wang, W., Yin, L., Li, M., Yu, Z., Chang, S., & Hou, F. (2023). Monitoring leaf area index of the sown mixture pasture through UAV multispectral image and texture characteristics. *Computers and Electronics in Agriculture, 214*, Article 108333. https://doi.org/10.1016/j.compag.2023.108333

Wang, Y., & Fang, H. (2020). Estimation of LAI with the LiDAR technology: A review. *Remote Sensing, 12*(20), 3457. https://doi.org/10.3390/rs12203457

Woodgate, W., Jones, S. D., Suarez, L., Hill, M. J., Armston, J. D., Wilkes, P., Soto-Berelov, M., Haywood, A., & Mellor, A. (2015). Understanding the variability in ground-based methods for retrieving canopy openness, gap fraction, and leaf area index in diverse forest systems. *Agricultural and Forest Meteorology, 205*, 83–95. https://doi.org/10.1016/j.agrformet.2015.02.012

Xiao, Z., Liang, S., Wang, J., Xiang, Y., Zhao, X., & Song, J. (2016). Long-time-series global land surface satellite leaf area index product derived from MODIS and AVHRR surface reflectance. *IEEE Transactions on Geoscience and Remote Sensing, 54*(9), 5301–5318. https://doi.org/10.1109/TGRS.2016.2560522

Xu, W., Yang, W., Chen, S., Wu, C., Chen, P., & Lan, Y. (2020). Establishing a model to predict the single boll weight of cotton in Northern Xinjiang by using high resolution UAV remote sensing data. *Computers and Electronics in Agriculture, 179*, Article 105762. https://doi.org/10.1016/j.compag.2020.105762

Yao, X., Wang, N., Liu, Y., Cheng, T., Tian, Y., Chen, Q., & Zhu, Y. (2017). Estimation of wheat LAI at middle to high levels using unmanned aerial vehicle narrowband multispectral imagery. *Remote Sensing, 9*(12), Article 1304. https://doi.org/10.3390/rs9121304

You, D., Gao, X., & Katayama, S. (2014). WPD-PCA-based laser welding process monitoring and defects diagnosis by using FNN and SVM. *IEEE Transactions on Industrial Electronics, 62*(1), 628–636. https://doi.org/10.1109/TIE.2014.2319216

Yuan, H., Yang, G., Li, C., Wang, Y., Liu, J., Yu, H., Feng, H., Xu, B., Zhao, X., & Yang, X. (2017). Retrieving soybean leaf area index from unmanned aerial vehicle hyperspectral remote sensing: Analysis of RF, ANN, and SVM regression models. *Remote Sensing, 9*(4), Article 309. https://doi.org/10.3390/rs9040309

Yuan, S., Stuart, A. M., Laborte, A. G., Rattalino Edreira, J. I., Dobermann, A., Kien, L. V. N., Thúy, L. T., Paothong, K., Traesang, P., Tint, K. M., San, S. S., Villafuerte, M. Q., II., Quicho, E. D., Pame, A. R. P., Then, R., Flor, R. J., Thon, N., Agus, F., Agustiani, N., … Grassini, P. (2022). Southeast Asia must narrow down the yield gap to continue to be a major rice bowl. *Nature Food, 3*(3), 217–226. https://doi.org/10.1038/s43016-022-00477-z

Zhang, J., Cheng, T., Guo, W., Xu, X., Qiao, H., Xie, Y., & Ma, X. (2021). Leaf area index estimation model for UAV image hyperspectral data based on wavelength variable selection and machine learning methods. *Plant Methods, 17*(1), 49. https://doi.org/10.1186/s13007-021-00750-5

Zhang, K., Ge, X., Shen, P., Li, W., Liu, X., Cao, Q., Zhu, Y., Cao, W., & Tian, Y. (2019). Predicting rice grain yield based on dynamic changes in vegetation indexes during early to mid-growth stages. *Remote Sensing, 11*(4), Article 387. https://doi.org/10.3390/rs11040387

Zhao, Q., Yu, S., Zhao, F., Tian, L., & Zhao, Z. (2019). Comparison of machine learning algorithms for forest parameter estimations and application for forest quality assessments. *Forest Ecology and Management, 434*, 224–234. https://doi.org/10.1016/j.foreco.2018.12.019

Zu, J., Yang, H., Wang, J., Cai, W., & Yang, Y. (2024). Inversion of winter wheat leaf area index from UAV multispectral images: Classical vs. deep learning approaches. *Frontiers in Plant Science, 15*, Article 1367828. https://doi.org/10.3389/fpls.2024.1367828

Authors and Affiliations

Chao Su[1] · Zaiying Ling[1] · Liwang Han[1] · Yanmin Shuai[2] · Jianguang Wen[3] · Xingwen Lin[2] · Haifeng Tang[4] · Alexandre Maniçoba da Rosa Ferraz Jardim[5] · Hoi Leong Lee[6] · Xuguang Tang[1]

✉ Xuguang Tang
xgtang@swu.edu.cn

1 Zhejiang Provincial Key Laboratory of Wetland Intelligent Monitoring and Ecological Restoration, Institute of Remote Sensing and Geosciences, Hangzhou Normal University, Hangzhou 311121, China

2 College of Geography and Environmental Sciences, Zhejiang Normal University, Jinhua 321004, China

3 State Key Laboratory of Remote Sensing Science, Aerospace Information Research Institute, Chinese Academy of Sciences, Beijing 100101, China

4 Shaoxing New Qingma Farm Co., Ltd., Shaoxing 312037, China

5 Department of Biodiversity, Institute of Biosciences, São Paulo State University UNESP, Av. 24A, 1515, Rio Claro, São Paulo 13506-900, Brazil

6 Faculty of Electronic Engineering & Technology, Universiti Malaysia Perlis, 02600 Arau, Perlis, Malaysia